

# Kelvin-Helmholtz Billows in the Troposphere and Lower Stratosphere Detected by the PANSY Radar

Yuichi Minamihara<sup>1</sup>, Kaoru Sato<sup>1</sup>, and Masaki Tutumi<sup>2</sup>

<sup>1</sup>University of Tokyo

<sup>2</sup>NIPR

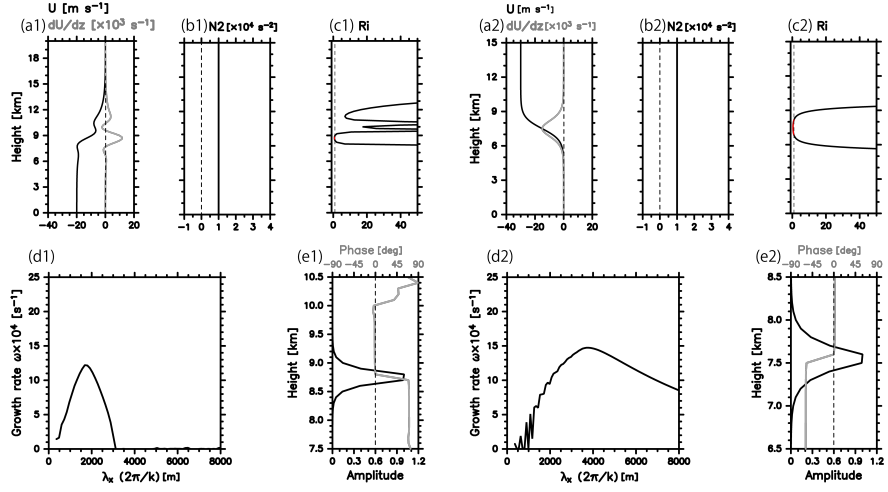
November 24, 2022

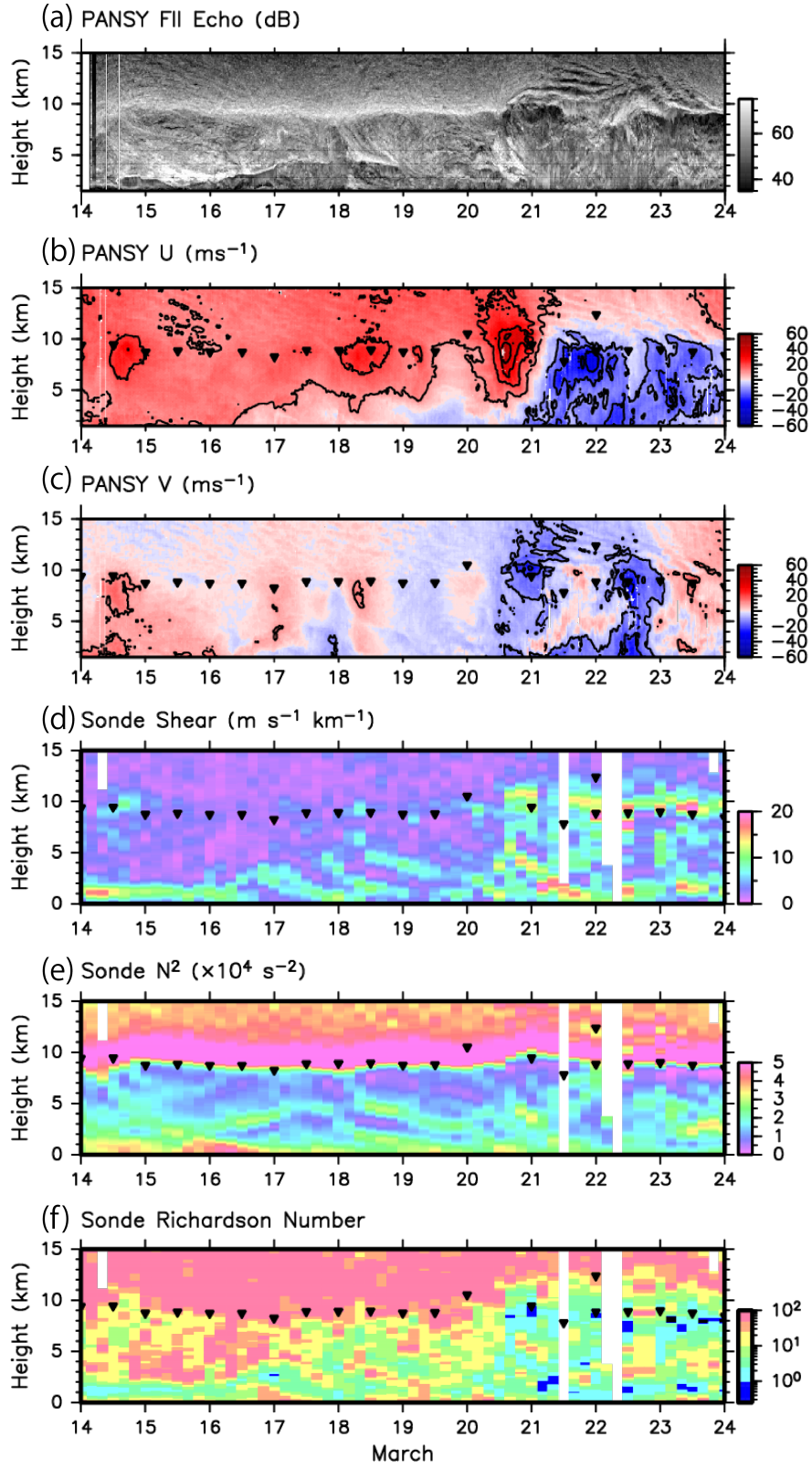
## Abstract

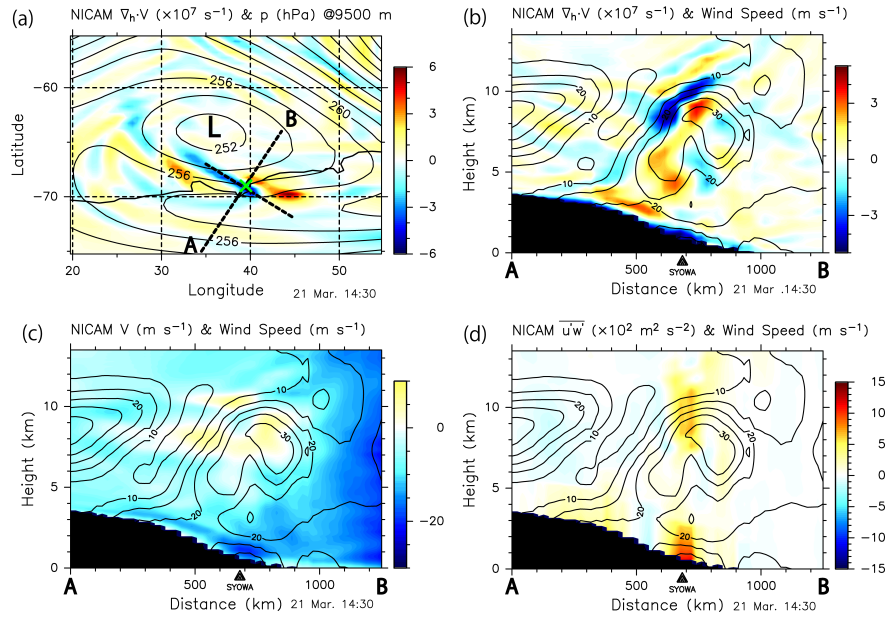
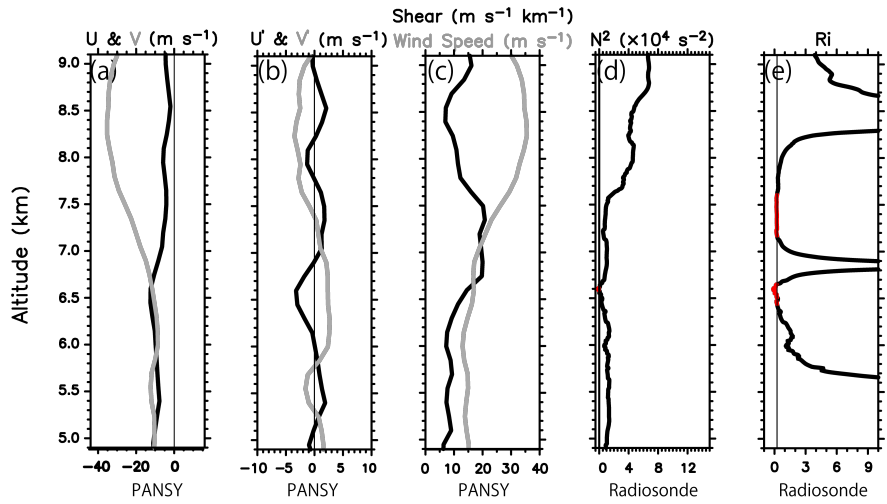
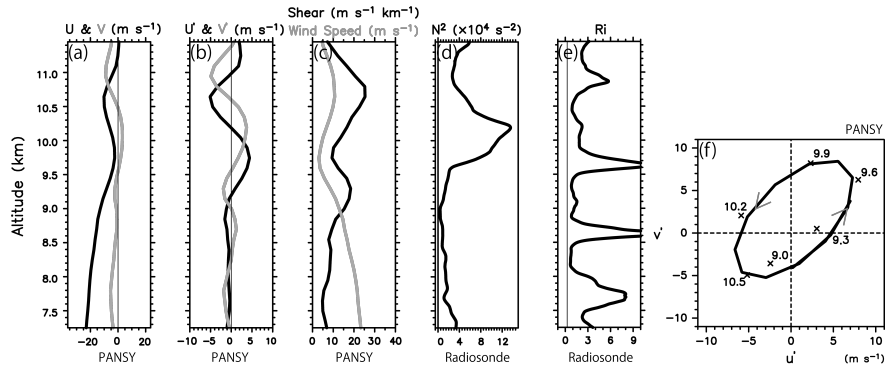
We conducted two 10-day observational campaigns in 2019 targeting turbulence in the troposphere and lower stratosphere by adopting a frequency domain radar interferometric imaging technique using Program of the Antarctic Syowa (PANSY) radar and radiosonde observations obtained at Syowa Station in the Antarctic. Overall, 73 cases of Kelvin-Helmholtz (K-H) billows were detected, and 2 characteristic cases were examined in detail. In the first case with the longest duration of  $\sim 6.5$  h, the K-H billows had thickness of  $\sim 800$  m and horizontal wavelength of  $\sim 2500$  m. According to a numerical simulation of the environmental conditions, continuously existing orographic gravity waves maintained strong vertical shear of the horizontal winds sufficient to cause the K-H instability. In the second case with the deepest thickness of  $\sim 1600$ m, the K-H billows had duration of  $\sim 1.5$  h and horizontal wavelength of  $\sim 4320$ m. Numerical simulation suggested that an enhanced upper-tropospheric jet associated with a well-developed synoptic-scale cyclone caused the K-H instability. Such background conditions, frequently observed in the Antarctic coastal region, are typical mechanisms for K-H excitation. Linear stability analysis also indicated that the characteristics of the observed K-H billows were consistent with the most unstable modes. Furthermore, static analysis was performed using data of all 73 observed cases. The characteristics of K-H billows observed at Syowa Station are similar to those observed over Japan. However, the weaker vertical shear and longer wave period of the K-H billows over Syowa Station reflect that the tropospheric jet over the Antarctica is not as strong as that over Japan.

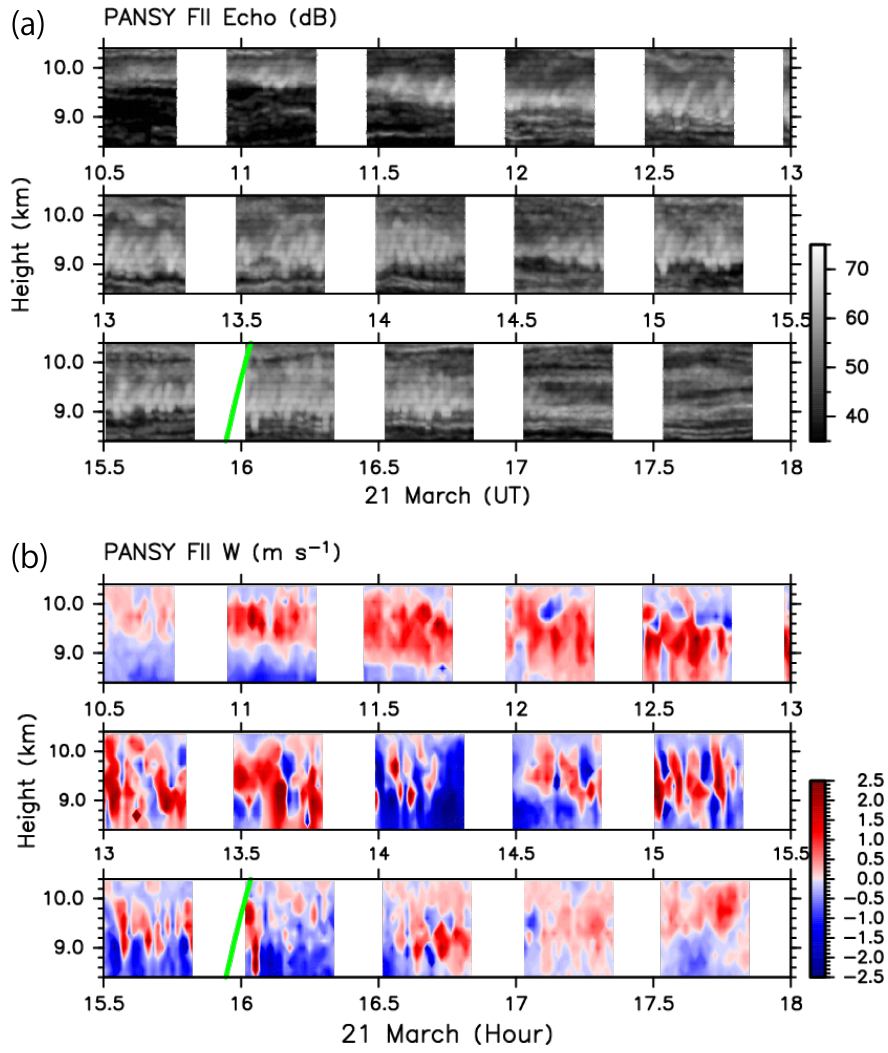
## Hosted file

essoar.10511059.1.docx available at <https://authorea.com/users/553206/articles/605010-kelvin-helmholtz-billows-in-the-troposphere-and-lower-stratosphere-detected-by-the-pansy-radar>









Yuichi Minamihara<sup>1</sup>, Kaoru Sato<sup>1</sup>, and Masaki Tsutsumi<sup>3</sup>

<sup>1</sup>Department of Earth and Planetary Science, Graduate School of Science, The University of Tokyo, Tokyo, Japan

<sup>2</sup>National Institute of Polar Research, Tachikawa, Japan

Corresponding author: Yuichi Minamihara (minamihara@eps.s.u-tokyo.ac.jp)

Key Points:

- Seventy-three Kelvin-Helmholtz billows were detected in PANSY radar observations using a frequency radar interferometric imaging technique
- Orographic gravity waves and well-developed cyclones unique to the Antarctic coastal region cause strong vertical shear
- Kelvin-Helmholtz billows in the coastal Antarctic region have comparable spatial scale and strength to those in the mid-latitudes

Abstract

We conducted two 10-day observational campaigns in 2019 targeting turbulence in the troposphere and lower stratosphere by adopting a frequency domain radar interferometric imaging technique using Program of the Antarctic Syowa (PANSY) radar and radiosonde observations obtained at Syowa Station in the Antarctic. Overall, 73 cases of Kelvin-Helmholtz (K-H) billows were detected, and 2 characteristic cases were examined in detail. In the first case with the longest duration of  $\sim 6.5$  h, the K-H billows had thickness of  $\sim 800$  m and horizontal wavelength of  $\sim 2500$  m. According to a numerical simulation of the environmental conditions, continuously existing orographic gravity waves maintained strong vertical shear of the horizontal winds sufficient to cause the K-H instability. In the second case with the deepest thickness of  $\sim 1600$  m, the K-H billows had duration of  $\sim 1.5$  h and horizontal wavelength of  $\sim 4320$  m. Numerical simulation suggested that an enhanced upper-tropospheric jet associated with a well-developed synoptic-scale cyclone caused the K-H instability. Such background conditions, frequently observed in the Antarctic coastal region, are typical mechanisms for K-H excitation. Linear stability analysis also indicated that the characteristics of the observed K-H billows were consistent with the most unstable modes. Furthermore, statical analysis was performed using data of all 73 observed cases. The characteristics of K-H billows observed at Syowa Station are similar to those observed over Japan. However, the weaker vertical shear and longer wave period of the K-H billows over Syowa Station reflect that the tropospheric jet over the Antarctica is not as strong as that over Japan.

1 Introduction

Kelvin-Helmholtz instability (KHI) is shear instability that occurs in a stratified fluid with strong vertical shear of the horizontal winds. It is well known that a necessary condition for KHI is that the Richardson number (Ri) must be  $< 0.25$  (e.g., Miles & Howard, 1964; Scorer, 1969). The Richardson number

can be estimated as follows:  $Ri = \frac{N^2}{|\frac{d\mathbf{U}}{dz}|^2}$ , where  $N$  is the buoyancy (Brunt-V is 1) frequency and  $|\frac{d\mathbf{U}}{dz}|$  is the magnitude of the vertical shear vector of the horizontal winds. As can be seen in the Ri formula, even if the atmosphere is stably stratified, a sufficiently large vertical shear  $|\frac{d\mathbf{U}}{dz}|$  can initiate instability. KHI is considered one of the main sources of clear air turbulence that affects the safety and comfort of air travel (e.g., Ralph et al., 1997).

Billows generated by KHI (K-H billows) can irreversibly mix and transport heat, momentum, and minor atmospheric constituents. K-H billows have a wavenumber vector parallel to the vertical shear vector, and these waves are eventually converted to turbulence (e.g., Browning & Watkins, 1970). Sometimes, K-H billows are visible as vortex rolls in thin cloud layers or on the limb of clouds (e.g., Browning & Watkins, 1970; Takayabu, 1992; Luce et al., 2018). Many studies have reported that K-H billows typically have thickness of 200–1000 m and horizontal wavelength of 1.5–4.0 km (Fukao et al., 2011 and references therein). It is also reported that KHI is associated with various atmospheric phenomena, such as gravity waves (GWs) (Fritts, 1979; Luce et al., 2008), air-flow over mountainous terrain (Geerts et al., 2010; Mahalov et al., 2007; Medina & Houze, 2016), tropospheric jets (Chilson et al., 1997; Klostermeyer & Rüster, 1980), cold fronts (Chapman & Browning, 1999; Geerts et al., 2006; Hardy et al., 1973; Samelson & Skillingstad, 2016; Takayabu, 1992), and mid-latitude cyclones (Trier et al., 2020; Wakimoto et al., 1992).

Mesosphere-stratosphere-troposphere (MST) radar observations of K-H billows started around 1980 (VanZandt et al., 1979; Luce et al., 2007; Fukao et al., 2011). In radar observations, K-H billows appear as “S-shaped” structures called “braids” or “cat’s eyes” (e.g., VanZandt et al., 1979). Stretched and compressed isentropic surfaces at the edge of billows provide irregularities of the refractive index of radar radio waves that result in strong echoes. In contrast, stirring and mixing of the isentropic surfaces near the center of billows reduce irregularities and the reflectivity of radar radio waves providing weak echoes. Observations by an MST radar can be conducted under any weather conditions, since the target of MST radars is mainly backscattering from Bragg-scale clear air turbulence. This is in contrast to Frequency-Modulated Continuous Wave radar observations that are limited to the planetary boundary layer, and cloud radar and lidar observations that require Mie/Rayleigh scattering by hydrometeors (e.g., Petre & Verlinde, 2004; Sassen, 2002).

In situ and direct measurements of turbulence have also been conducted. For example, Schneider et al. (2015) performed observations using the Leibniz-Institute Turbulence Observations in the Stratosphere (LITOS) high-speed-sampling (8 kHz) turbulence measurement instrument (Theuerkauf et al., 2011). The LITOS provides the entire turbulence spectrum over the viscous subrange that enables direct estimation of the turbulent energy dissipation rate ( $\varepsilon$ ). They confirmed that the mean values of  $\varepsilon$  obtained by the LITOS were consistent with those inferred from radiosonde observations using the Thorpe

method. Luce et al. (2018) performed simultaneous observations with the MU radar (34.9°N, 136.1°E), which is an MST radar, using the frequency-domain radar interferometric imaging (FII) technique and an unmanned aerial vehicle (UAV) equipped with a variety of high-resolution sensors for pressure (44.4 Hz), temperature (100 Hz), and wind speed (100 Hz) (Kantha et al., 2017). They estimated  $\varepsilon$  directly from the frequency power spectra of temperature fluctuations observed by the UAV. It was shown that the  $\varepsilon$  values estimated from the UAV observations accorded well with those from the MU radar. Grasmick and Geerts (2020) elucidated the generation mechanisms of K-H billows in airflow over complex mountain terrains using observations from a 3-mm Doppler radar aboard an aircraft. The range resolution of the radar was  $\sim 40$  m. They observed K-H billows not only upwind of a terrain barrier but also in the area immediately leeward of steep terrain at various altitudes including the free atmosphere, upper boundary layer, and near the surface.

Statistical studies of turbulence in the Antarctic have been conducted using observations by the Program of the Antarctic Syowa (PANSY) radar (Sato et al., 2014). Kohma et al. (2019) performed statistical comparison of  $\varepsilon$  derived from PANSY radar observations and that deduced from operational radiosonde observations using the Thorpe method. They found a characteristic height dependence of  $\varepsilon$  that is larger in the stratosphere than in the troposphere. They also indicated that a moderate maximum of  $\varepsilon$  is evident just above the tropopause (at  $z = \sim 11$  km) from August to November, while a weak local maximum is observed in the lower stratosphere from February to April. Moreover, they also reported that the value of  $\varepsilon$  derived from radiosonde observations is approximately 2–5 times larger than that deduced from the PANSY radar depending on height.

To date, few case studies have examined K-H billows in the polar region using direct observations. Furthermore, research using the remote sensing techniques such as radar or lidar to examine the atmospheric phenomena that cause KHI is lacking, even in low- and mid-latitude regions where such observations can be obtained relatively easily. The objectives of this study were to detect K-H billows for the first time in the Antarctic troposphere and lower stratosphere directly by the PANSY radar observations using the FII technique, and to clarify the dynamical characteristics and excitation mechanisms of K-H billows.

This paper is organized as follows. Methodologies of observations and numerical simulations including data descriptions are presented in Section 2. In Section 3, two case studies of characteristic K-H billows are examined. Additionally, the statistical characteristics of all 73 detected K-H billows are analyzed. The most unstable modes of the observed conditions for the two case studies, obtained from linear stability analysis, are compared with the observations in Section 4.1. The development process of the cyclone that caused the KHI is discussed in Section 4.2. Finally, a summary and the derived conclusions are presented in Section 5.

## 2 Data and Methodology

Two 10-day continuous observational campaigns using the PANSY radar and radiosondes targeting fine atmospheric turbulence were performed at Syowa Station in the Antarctic. The first campaign covered the time period of 14–24 March 2019 and the second campaign covered the period of 2–12 August 2019. Note that among previous MST radar observations using the FII technique (e.g., Luce et al., 2001), the campaigns conducted in this study were unprecedentedly long and continuous. Numerical simulations using the Nonhydrostatic Icosahedral Atmospheric Model (NICAM; Satoh et al., 2008; 2014) were also performed to investigate the spatial structures of GWs and cyclones considered related to the generation mechanisms of K-H billows.

## 2.1 PANSY Radar Observations

The PANSY radar was installed at Syowa Station (69.0°S, 39.6°E) in early 2011. This radar is the first MST/Incoherent Scatter radar in the Antarctic (Sato et al., 2014). The PANSY radar is a monostatic pulse VHF clear air Doppler radar which is an active phased array system consisting of 1,045 crossed-Yagi antennas.

Two observational modes were used alternately during the campaigns: a standard stratosphere-troposphere (ST) observation mode for 7 min and the FII mode for 22 min. The central frequency of the PANSY radar is 47 MHz. The standard ST mode uses five beams: a vertical beam and four oblique beams tilted to the east, west, north, and south with a zenith angle of 10°. Line-of-sight velocity, echo power, and spectral width ( $\sigma$ ) of the scattering echoes from each beam were obtained at a time interval ( $\Delta t$ ) of approximately 220 s and range resolution ( $\Delta r$ ) of 150 m. The accuracy of the line-of-sight velocity is reasonably high ( $\sim 0.1 \text{ m s}^{-1}$ ). For details of the methods for estimations of three-dimensional winds and momentum fluxes, see section 2.1 of Minamihara et al. (2020).

The value of  $\varepsilon$ , which is a measure of turbulence intensity, was estimated using  $\sigma$  (e.g., Sato & Woodman, 1982; Hocking, 1983; Kohma et al., 2019). The echo spectra versus line-of-sight Doppler velocity have a finite width owing to the motion of the turbulent eddies having the Bragg scale (half of the radar wavelength:  $\lambda \approx 3 \text{ m}$ ) in the targeted volume range with depth of  $\sim 150 \text{ m}$  along the beam (Fukao & Hamazu, 2014). Contaminations of beam broadening  $\sigma_{\text{beam}}^2$ , shear broadening  $\sigma_{\text{shear}}^2$ , and time broadening  $\sigma_{\text{time}}^2$  to the spectral width  $\sigma_{\text{obs}}^2$  should be properly extracted to obtain the contribution of turbulence  $\sigma_{\text{turb}}$ :

$$\sigma_{\text{turb}}^2 = \sigma_{\text{obs}}^2 - \sigma_{\text{beam}}^2 - \sigma_{\text{shear}}^2 - \sigma_{\text{time}}^2 . \quad (1)$$

$$v'^2 = \frac{\sigma_{\text{turb}}^2 (\frac{\lambda}{2})^2}{(2 \ln 2)} . \quad (2)$$

$$\varepsilon \approx c_R v'^2 N, \quad (3)$$

where  $v'^2$  is the velocity variance. We used a value of  $N$  derived from a radiosonde observation performed at the nearest time, and a value of 0.45 was adopted for  $c_R$  following Hocking (1999). It is worth noting that the beam broadening component ( $\sigma_{\text{beam}}$ ) was extracted using a strict method developed by Nishimura et al. (2020), which can be applied to the irregular antenna distribution of the PANSY radar. The effect of time broadening ( $\sigma_{\text{time}}$ ) was neglected because of its small magnitude in comparison with that of the other broadenings (Nastrom & Eaton, 1997); see Kohma et al. (2019) for further details.

In the FII mode, Doppler spectra were obtained at five different frequencies (47 MHz, 47 MHz $\pm$ 500 kHz, and 47 MHz $\pm$ 250 kHz) in the vertical direction. The collected data were processed using the adaptive Capon processing method (Luce et al., 2001; Palmer et al., 1999). It provided echo power and line-of-sight velocity, i.e., vertical wind ( $w$ ), with range resolution finer than the transmitted subpulse width (1 s) (e.g., Luce et al., 2006). The height region of  $z = 1.5$ –15.0 km was chosen as the analysis height region. The data of the FII mode had resolution of  $\Delta t = \sim 13$  s and  $\Delta r = \sim 9.3$  m. Fukao et al. (2011) stated that a value of  $\Delta t$  shorter than 80 s is necessary to detect the structure of K-H billows, which is a condition satisfied by the observations obtained in this study.

Figures 1 and 2 shows time-height sections of (a) echo power from the PANSY FII mode observation, and (b) zonal ( $u$ ) and (c) meridional winds ( $v$ ) from the PANSY standard mode observations from the first and second observational campaigns, respectively. Various atmospheric phenomena with different temporal and spatial scales are evident in Figures 1a and 2a. However, K-H billows are not obvious in these figures because their structure is so small relative to the scale of the section. During 14–20 March, a strong echo layer is continuously visible at  $z = 9.0$ –10.0 km, corresponding to the tropopause. In the upper troposphere and lower stratosphere, wave-like structures with vertical wavelength of 1.5–2.0 km are evident during 20–23 March. These wave-like structures are also apparent in the horizontal winds. During this period, the continuous strong echo layer corresponding to the tropopause is temporarily disappeared,  $u$  changes from eastward to westward, and strong southward winds of  $\sim 40$  m  $s^{-1}$  blow at  $z = 9.0$ –10.0 km. The change in wind direction and increase in horizontal wind speed are associated with a cyclone that approached Syowa Station, as described in detail later. During 14–20 March and 4–9 August, strong echo layers continuously exist at  $z = 2.0$ –6.0 km, although those present in August are not as clear as those seen in March.

## 2.2 Radiosonde Observations

During the campaigns, radiosonde observations were performed at 4-h intervals (i.e., 03:30, 07:30, 11:30, 15:30, 19:30, and 23:30 UTC). The buoyancy force of each balloon was adjusted to ensure an ascent speed of 5.0–6.0 m  $s^{-1}$ . The ra-

diasondes observed temperature, horizontal winds, and humidity at 1-s intervals. Overall, 117 radiosonde observations were performed successfully, although for four launches (11:30 UTC on 21 March and 03:30, 07:30, and 15:30 UTC on 22 March) failed owing to strong near-surface winds with speed  $>20 \text{ m s}^{-1}$ .

It is worth noting that winds in the height region of  $z < 1.5 \text{ km}$  cannot (can) be observed by the PANSY radar (radiosondes). To investigate possible KHI, vertical shear ( $|\frac{d\mathbf{U}}{dz}| = \sqrt{(\frac{du}{dz})^2 + (\frac{dv}{dz})^2}$ ),  $N^2$ , and Ri were estimated using the radiosonde observations, which were smoothed by taking a 150-m running mean in the vertical.

Figures 1d–f and 2d–f show time-height sections of  $|\frac{d\mathbf{U}}{dz}|$ ,  $N^2$  and Ri for the two observational campaigns, respectively. In March, discontinuous increase in  $N^2$  with height is observed in the height region of  $z = 8.0\text{--}10.0 \text{ km}$  throughout the observational period. This structure corresponds to the tropopause inversion layer (Birner et al., 2006; Tomikawa et al., 2009), which is evident from December to April in the Antarctic. Conversely, such increase in  $N^2$  around the tropopause is relatively indistinct in August when daylight hours are short. The strong echo layer corresponding to the tropopause is also obscure in August. In the upper troposphere,  $N^2$  sometimes takes relatively small values in both months. During these periods, Ri is  $<1.0$ . Moreover, during 20–23 March, when the cyclone approached Syowa Station,  $|\frac{d\mathbf{U}}{dz}|$  is large and Ri is  $<1.0$  near the surface and in the upper troposphere. Additionally, during 14–20 March, thin layers with large  $N^2$  values are observed in the height region of  $z = 2.0\text{--}5.0 \text{ km}$ . Slightly below this height region,  $|\frac{d\mathbf{U}}{dz}|$  is large and  $N^2$  is small, resulting in relatively small Ri. These regions correspond well to the thin and strong echo layers observed in Figure 1a.

### 2.3 NICAM simulations

To examine the spatial structures of the mesoscale and synoptic-scale atmospheric phenomena such as GWs and cyclones that can provide the conditions for KHI, NICAM was used to perform numerical simulations. NICAM is a global cloud-resolving model with a nonhydrostatic dynamical core developed for icosahedral grids modified by the spring dynamics method (Tomita & Satoh, 2004).

The NICAM setup adopted in this study was largely based on that of Shibuya and Sato (2019), in which the model extends to the height of  $z = \sim 80 \text{ km}$  with 300-m vertical grid spacing and has an almost uniform horizontal spatial grids with resolution of  $\sim 28 \text{ km}$  for the mid- and high-latitude regions of the Southern Hemisphere to simulate GWs. In the present study, modification was made to the vertical grid, i.e., vertical grid spacing ( $\Delta z$ ) was  $\sim 100 \text{ m}$  from the surface to  $z = 40 \text{ km}$  (386 layers), and sponge layers were placed above  $z = 35 \text{ km}$  to suppress unrealistic wave reflection from the model top. We adopted the horizontal grid developed by Shibuya et al. (2016), as did Shibuya and Sato (2019). This grid is designed to concentrate the grid points south of  $30^\circ\text{S}$  such that the grid points are spaced almost equally in the region. We took a grid

with grid-level 8, corresponding to a horizontal grid spacing of  $\sim 18$  km to the south of  $30^{\circ}\text{S}$ .

The Modern-Era Retrospective Analysis for Research and Applications version 2 (MERRA-2) dataset (Gelaro et al., 2017) was used to provide the initial atmospheric conditions. The initial values for the land surface and slab ocean were obtained by interpolation from the  $1.0^{\circ}$  gridded National Centers for Environmental Prediction (NCEP) final analysis. It should be emphasized that cumulus and GW parameterizations and nudging methods were not used in the present simulation.

Time integrations were performed for a limited period during which the model could realistically simulate the atmosphere and were repeated to cover the entire observational campaigns, similar to Plougonven et al. (2013) and Shibuya and Sato (2019). A series of 3–4-day simulations were performed for which adjacent runs overlapped by 1 day. The data from the last 2–3 days of each run were used for analysis because 1 day was needed for the spin-up of the model. This method reduces discrepancy from the real atmosphere and allows the model to simulate GWs freely, although discontinuity does appear between runs. The time step of the integration was 8 s, and the model output was stored every 30 min as a snapshot. For 20–24 March, when a cyclone approached Syowa Station, we performed additional simulations with a 2-day integration time to carefully examine the cyclone development and other related phenomena. In these simulations, only the last 1 day of each run was used for analysis. Such short free-run integrations reproduced the location of the cyclone more realistically.

For the horizontal wind, not only the winds on synoptic and larger scales, but also the GW-like structures in the upper troposphere and lower stratosphere were all well reproduced in the NICAM simulations. However, although the structures of vertical wind disturbances in the lower troposphere observed by the PANSY radar were broadly reproduced in the NICAM simulations, their amplitude was approximately one-fifth that in the real atmosphere. Small-scale topography that cannot be fully reproduced by the model is considered important for reproducing vertical wind disturbances. Thus, we analyzed the spatial structures of the atmospheric phenomena likely to cause K-H billows based on the horizontal winds and temperature simulated by NICAM.

### 3 Results

S-shaped echo patterns are one of the characteristics of K-H billows. During the two campaigns, 73 cases were detected visually in the high-resolution time-height cross sections of echo power observed by the PANSY FII mode. Among them, the spatial structures and wave periods of the K-H billows were estimated for cases whose vertical scale and duration were greater than 150 m and 1000 s, respectively. Before undertaking statistical analysis (Section 3.2), we examined two observed cases considered characteristic in terms of their dynamical structure and excitation mechanisms (Sections 3.1.1 and 3.1.2): Case A is the one with the longest duration and Case B is the one with the deepest structure of

the K-H billows.

### 3.1 Case Studies

#### 3.1.1 Longest Duration Case (Case A)

The K-H billows for Case A were observed in the height region of  $z = 8.8\text{--}10.2$  km for  $\sim 6.5$  h from 11:00–17:30 UTC on 21 March. Figures 3a and 3b shows time-height cross sections of echo power and vertical wind ( $w$ ) from the PANSY radar FII mode observations, respectively. A strong echo layer is observed at  $z = \sim 9.8$  km at around 10:36 UTC, and the thickness of the layer increases in the height region of  $z = 9.6\text{--}10.0$  km after 11:30 UTC. By 12:12 UTC, the layer descends to  $z = \sim 8.7$  km and the wave-like structures become clearer. After 12:30 UTC, the layer thickens in the height region of  $z = 8.8\text{--}9.8$  km and retains its structure with S-shaped patterns until 16:48 UTC, except for temporary thinning and weakening of the echo patterns at around 14:30 UTC. The K-H billow structure disappears rapidly at around 17:00 UTC.

The mean thickness and wave period for Case A are  $\sim 800$  m and  $\sim 285$  s, respectively. Vertical wind disturbances shown in Figure 3b exhibit phase shift between regions above and below the central altitude of the KH billows. The magnitude of the vertical wind disturbances is reasonably strong and reaches  $3.43\text{ m s}^{-1}$  at around 13:33 UTC. The amplitude of the vertical wind disturbances is small at the beginning and end of Case A, when the S-shaped echo patterns are not clear.

Figure 4a–c shows vertical profiles of horizontal winds ( $u$  and  $v$ ), horizontal wind disturbances ( $u'$  &  $v'$ ) with vertical wavelength ( $\lambda_z$ ) shorter than 3 km, and  $|\frac{d\mathbf{U}}{dz}|$  from the PANSY radar standard mode observation at 14:01 UTC on 21 March, respectively. Vertical profiles of  $N^2$  and Ri observed by the radiosonde launched at 15:30 UTC on 21 March are also shown in Figure 4d and 4e, respectively. In the height region of  $z = 9.0\text{--}9.5$  km, where the K-H billows are clearly observed, the background wind direction is westward, i.e., almost parallel to the eastward shear vector of the horizontal winds. The background wind speed is  $\sim 8.8\text{ m s}^{-1}$ , while the wave period of the observed K-H billows is  $\sim 285$ s. Assuming that the K-H billows are advected by the background wind, their horizontal wavelength is estimated at  $\sim 2500$  m, which corresponds to an aspect ratio of  $\sim 0.32$ .

A wave-like disturbance of the horizontal winds with vertical wavelength  $\lambda_z$  of  $\sim 1.5$  km is seen in the height region of  $z > 8.5$  km (Figure 3b). The amplitude of this wave-like disturbance is reasonably large below the weak wind layer at around  $z = 11.5$  km. Owing to the existence of this wave-like structure,  $|\frac{d\mathbf{U}}{dz}|$  is large in the height regions of  $z = 8.9\text{--}9.6$  and  $10.2\text{--}11.3$  km. However,  $N^2$  is large ( $> 8.0 \times 10^{-4}\text{ s}^{-2}$ ) at  $z = 9.7\text{--}10.4$  km and small ( $\sim 1.0\text{--}2.0 \times 10^{-4}\text{ s}^{-2}$ ) at  $z < 9.5$  km. Reflecting these profiles of  $|\frac{d\mathbf{U}}{dz}|$  and  $N^2$ , Ri is locally small (i.e., close to or less than 1.0) in the height region of  $z = 8.9\text{--}9.5$  km. This height region corresponds well to the regions in which the K-H billows are observed.

We performed a hodograph analysis (Figure 2f) for  $u'$  and  $v'$  having  $\lambda_z$  of

300 m to 3 km (e.g., Sato, 1994; Minamihara et al., 2018), assuming that the wave-like structure was due to an inertia GW. The result indicates vertical and horizontal wavelengths estimated at 1.6 and 145 km, respectively. The ground-based horizontal phase velocity is  $2.3 \text{ m s}^{-1}$ , and the wavenumber vector points northeastward. The direction of the wavenumber vector is uniquely determined from the phase relationship of the vertical and horizontal wind disturbances. The hodograph rotates counterclockwise with altitude, which is a property of inertia-GWs with an upward group velocity in the Southern Hemisphere. The wave-like disturbances accompanying the strong vertical shear are likely due to an orographic inertia GW, considering the following three points: the small ground-based horizontal velocity, the amplification of horizontal wind components below the weak wind layer, and the upward vertical group velocity.

We examined data from the NICAM numerical simulation to confirm whether the disturbances have horizontal structure consistent with an orographic inertia GW. As stated before, the wave-like structures observed by the PANSY radar were well simulated by NICAM. Results of a hodograph analysis for the wave-like disturbances appearing in the NICAM simulation indicate that the wave parameters are comparable with those estimated for the PANSY radar observations (not shown).

Figure 5a shows a longitude-latitude cross section of horizontal wind divergence ( $\nabla_h \cdot v_h$ ) and pressure ( $p$ ) at  $z = 9.5 \text{ km}$  at 14:30 UTC on 21 March. A cyclone is located  $\sim 500 \text{ km}$  to the north-northwest of Syowa Station. A strong wave packet having a northeast-southwest wavenumber vector is clearly observed near Syowa Station. The wave packet extends to the south of the cyclone along the Antarctic coast. Figure 5b shows horizontal-height cross sections of  $\nabla_h \cdot v_h$  and horizontal wind speed along the A–B line shown in Figure 5a. The horizontal wind divergence is enhanced below  $z = \sim 12.0 \text{ km}$  where the horizontal wind speed is weak ( $\sim 10 \text{ m s}^{-1}$ ). The phase lines of large  $\nabla_h \cdot v_h$  are tilted northeastward (toward B) with height. A strong southwestward wind exceeding  $20 \text{ m s}^{-1}$ , which is associated with the cyclone, blows up the slope of the Antarctic continent (Figure 5c). The observed phase structure of the wave packet observed in Figure 5b is consistent with the orographic GWs generated by the strong southwestward wind near the surface. Figure 5d shows the vertical flux of zonal momentum ( $\overline{u'w'}$ ) in the same section as shown in Figure 5b. The momentum flux is also enhanced ( $\sim +8 \text{ m}^2 \text{ s}^{-2}$ ) below the weak wind layer, similar to  $\nabla_h \cdot v_h$ . Strong positive  $\overline{u'w'}$  is also directly observed by the PANSY radar at the same time (not shown). The magnitude of  $\overline{u'w'}$  estimated by the PANSY radar observations amounts to  $\sim 80 \text{ mPa}$ , which corresponds to the top 1% or less of the momentum fluxes for the height region of  $z = 9.0\text{--}10.5 \text{ km}$  identified through statistical analysis of PANSY radar data over a year (Minamihara et al., 2020). These characteristics strongly support our inference that the K-H billows in Case A were likely caused by strong vertical shear associated with orographic GWs. The long duration of the K-H billows in Case A can be explained by the near-stationary phase structure that orographic GWs should have and the con-

tinuous generation of orographic GWs by a slow moving synoptic-scale cyclone with southwestward phase velocity of  $\sim 20 \text{ km h}^{-1}$ .

### 3.1.2 Deepest Structure Case (Case B)

The K-H billows of Case B were observed in the height region of  $z = 6.2\text{--}7.8$  km during 10:54–12:36 UTC on 22 March. Time-height sections of echo power and  $w$  from the PANSY radar FII mode observations are shown in Figure 6a and 6b, respectively. A strong echo layer first appears at  $z = \sim 7.7$  km at around 10:54 UTC. At around 11:18 UT, the strong echo layer becomes deeper in the height region of  $z = 6.8\text{--}7.8$  km, and the S-shaped structure becomes more distinct. At around 11:48 UTC, the S-shaped pattern becomes clearer and expands substantially in the height region of  $z = 6.0\text{--}7.8$  km. After 12:30 UTC, the wave period of the K-H billows becomes shorter, and the S-shaped echo gradually becomes shallower. Eventually, the S-shape becomes obscure and hardly recognizable. The mean thickness and wave period at round 11:54 UTC are  $\sim 1600$  m, and  $\sim 240$  s, respectively.

Reasonably strong vertical wind disturbances with maximum amplitude of  $3.63 \text{ m s}^{-1}$  are observed at around 11:55 UTC when the deep and clear S-shaped structures are observed. The vertical wind disturbances are clear in the height region of  $z = 5.0\text{--}9.0$  km, which is deeper than the S-shaped echo pattern. Figure 6c shows a magnified view of  $w$  overlaid on the echo power for the period 11:48–12:06 UTC on 22 March. Over time, the  $w$  fluctuations change their sign at the upper and lower parts of the strong S-shaped echoes, and exhibit phase discontinuity by  $60\text{--}90^\circ$  at the height of  $z = \sim 7.0$  km.

Vertical profiles of  $u$  and  $v$ ,  $u'$  and  $v'$ , and  $|\frac{d\mathbf{U}}{dz}|$  from the PANSY radar standard mode observation at 12:00 UTC on 22 March are shown in Figure 7a–c, respectively. Vertical profiles of  $N^2$  and Ri observed by the radiosonde launched at 11:30 UTC on 22 March are also shown in Figure 7d and 7e, respectively. In the height region of  $z > 6.0$  km, southward winds are dominant and the strong wave-like wind disturbances observed for Case A are absent, suggesting different a generation mechanism of KHI in Case B. The vertical shear of horizontal winds is large in the height region of  $z = 6.6\text{--}7.6$  km. The wind and shear vectors are almost parallel in the height regions of  $z = 6.8\text{--}7.8$  km where the strong K-H billows are observed. Thus, considering that the observed K-H billows is advected by the background horizontal wind speed, which is  $\sim 18.0 \text{ m s}^{-1}$  near the center of the K-H billows, we can estimate that the horizontal wavelength is  $\sim 4320$  m. Therefore, the aspect ratio is  $\sim 0.37$ .

Owing to the substantial shear below the enhanced wind mentioned above, Ri is locally smaller than 0.25 at the height regions of  $z = 6.4\text{--}6.6$  and  $z = 7.1\text{--}7.6$  km, as shown by red color. These height regions correspond well to the regions in which the K-H billows are observed (Figure 6). The sharp increase of Ri at the height of  $z = \sim 6.8$  km is caused by weakening of  $|\frac{d\mathbf{U}}{dz}|$ , which was observed only by the radiosonde (not shown), and not by the PANSY radar. These differences likely reflect the fact that the radiosonde drifted by the strong westward wind

away from the horizontal location of the PANSY radar which observes almost vertically.

The NICAM simulation output was used to examine the spatial structure of the southward jet in the height region of  $z = 6.6\text{--}7.6$  km with strong vertical shear. Figure 8a shows a longitude-latitude cross section of  $\nabla_h \cdot v_h$  and  $p$  at  $z = 7.0$  km at 12:30 UTC on 22 March. A cyclone is located  $\sim 500$  km northwest of Syowa Station. This cyclone is the same one that caused the orographic GWs over Syowa Station in Case A. However, in contrast to Case A, wave-like structures are not evident over Syowa Station but are dominant to its west. Horizontal-height cross sections of  $v$ ,  $|\frac{dU}{dz}|$ , and Ri along a radial direction of the cyclone, i.e., line A–B depicted in Figure 8a, at 12:30 UTC on 22 March are shown in Figure 8b–d, respectively. They are overlaid with contours of horizontal wind speed. Above Syowa Station, a narrow southward jet is localized at the height region of  $z = 7.0\text{--}10.0$  km. Vertical shear is strong both above and below the jet, i.e., at  $z = 7.0\text{--}8.0$  km and  $z = \sim 9.0$  km, and thus Ri is relatively small. The K-H billows in Case B were observed by the PANSY radar in the lower part of the jet in the height region of  $z = 7.0\text{--}8.0$  km. Thus, the K-H billows in Case B were excited by the vertical shear below the local upper-tropospheric jet associated with the cyclone.

### 3.2 Statistical Characteristics

Statistical analysis was performed for all 73 cases of K-H billows detected during the two observational campaigns. Note that this study is the first study to report the statistical characteristics of K-H billows in the Antarctic region. Figure 9a shows a histogram of the K-H billows observed for each height region. Approximately 60% cases were detected within the lower most parts of the observational height region ( $z < 4.0$  km), and these cases were observed throughout the entire period. In the height region in which these K-H billows were detected,  $|\frac{dU}{dz}|$  is large. Additionally, northeasterly winds blew below the lower part of these height regions, which likely corresponded to katabatic winds from the Antarctic continent. In contrast, K-H billows in the upper troposphere and lower stratosphere were seen mainly on 20–23 March. In particular, only two cases were detected in the height region of  $z > 11$  km during 21–22 March (which were not Case A and Case B), which is when the cyclone was situated closest to Syowa Station. Figure 9 also shows histograms of (b) wave period, (c) depth, (d) wavelength, and (e) aspect ratio of the observed K-H billows, and (f) vertical shear from the PANSY radar standard mode observation, (g)  $N^2$ , and (h) Ri of the background fields. Fukao et al. (2011) performed statistical analysis for 271 cases of K-H billows detected by the MU radar ( $34.9^\circ\text{N}$ ,  $136.1^\circ\text{E}$ ). Table 1 summarizes the mean and median values of parameters obtained by the present study and those obtained by Fukao et al. (2011).

The mean (median) value of the wave period of the K-H billows is 177 s (162 s) and most cases have wave periods of 120–280 s. The mean (median) value of vertical thickness and horizontal wavelength is 559 m (500 m) and 2019 m (1837 m), respectively. Furthermore, the aspect ratio, which corresponds to the ratio of

the vertical thickness to the horizontal wavelength, has at mean (median) value of 0.34 (0.27). For the background field, the mean (median) value of  $|\frac{dU}{dz}|$  from the PANSY radar observations is  $13.1 \text{ m s}^{-1} \text{ km}^{-1}$  ( $12.3 \text{ m s}^{-1} \text{ km}^{-1}$ ). The mean (median) values of  $N^2$  and Ri estimated from the radiosonde observations are  $0.87 \times 10^{-4} \text{ s}$  ( $0.72 \times 10^{-4} \text{ s}$ ) and 1.07 (1.17), respectively. There are cases in which Ri exceeds 0.25, probably because these parameters were estimated using the nearest radiosonde observations and not by direct observations in the K-H billow regions. Fukao et al. (2011) reported that the mean (median) values of wave period, depth, horizontal wavelength, and vertical shear are 90 s (78 s), 620 m (200 m), 2600 m (2700 m), and  $21.4 \text{ m s}^{-1} \text{ km}^{-1}$  ( $23.4 \text{ m s}^{-1} \text{ km}^{-1}$ ) for the MU radar observations. They also reported the mean value of the aspect ratio as 0.22.

Depth, horizontal wavelength, and aspect ratio of K-H billows determined in the present study using the PANSY radar observations are similar to those derived from the MU radar observations by Fukao et al. (2011). However, the wave periods of the billows observed by the PANSY radar, are approximately twice those derived from the MU radar. This is likely due to weaker advection by the background wind over Syowa Station than over Shigaraki, reflecting the difference in the latitudinal location relative to the upper tropospheric jet.

Statistical analysis was also performed separately for the K-H billows observed in the first campaign in March (#48) and in the second campaign in August (#25) (not shown). There was no significant difference in any parameters associated with the K-H billows between March and August, although the  $\log_{10} \varepsilon$  value was slightly larger in March ( $\sim 0.10$ ) than in August ( $\sim 0.32$ ).

Figure 9i shows a histogram of  $\varepsilon$  for the entire observational time-height region (gray) and  $\varepsilon$  in the region where the K-H billows were observed (black). It indicates that the S-shaped echo patterns captured visually correspond well to the regions of active turbulence. However, it is worth noting that not all regions with intense turbulence correspond to K-H billows. The values of  $\varepsilon$  in the K-H billows estimated by the PANSY radar are consistent with those estimated by other mid-latitude observations including the MU radar (Figure 13b in Fukao et al., 2011).

## 4 Discussion

### 4.1 Most Unstable Mode Expected from Linear Theory

Following the theoretical two-dimensional linear stability analysis used in Takayabu (1992), we obtained the most unstable mode for idealized vertical profiles of horizontal winds ( $U_o(z)$ ) and the Brunt-V is l frequency squared ( $N^2(z)$ ), which mimic the Case A and Case B profiles. The linearized inviscid Boussinesq equations are given as follows:

$$\frac{\partial u}{\partial x} + \frac{\partial w}{\partial z} = 0, \quad (4-1)$$

$$\left( \frac{\partial}{\partial t} + U_o \frac{\partial}{\partial x} \right) u + \frac{\partial U_o}{\partial z} w + \frac{1}{\rho_o} \frac{\partial p}{\partial x} = 0, \quad (4-2)$$

---


$$\frac{\partial u}{\partial x} + \frac{\partial w}{\partial z} = 0 , \quad (4-1)$$


---

$$\left( \frac{\partial}{\partial t} + U_o \frac{\partial}{\partial x} \right) w + \frac{1}{g} \frac{\partial p}{\partial z} - g \frac{\theta}{\theta_o} = 0 , \quad (4-3)$$

$$\left( \frac{\partial}{\partial t} + U_o \frac{\partial}{\partial x} \right) \theta + \frac{N_o^2}{g} \theta_o w = 0 , \quad (4-4)$$

$$N^2 = \frac{g}{\theta_o} \frac{\partial \theta_o}{\partial z} , \quad (4-5)$$


---

where  $u$  and  $w$  are the horizontal and vertical wind perturbations, respectively,  $\theta$  is a potential temperature perturbation, and  $\theta_o$  is a potential temperature of the basic field. The notation for these equations differs from that used in other sections. Gravity acceleration is shown as  $g$ . From (4-1), we can define the stream function  $\Psi$  as follows:

---


$$u = \frac{\partial \psi}{\partial z}, \quad w = -\frac{\partial \psi}{\partial x} . \quad (5)$$


---

Eliminating the terms including  $p$  by combining (4-2) and (4-3) yields the followings:

---


$$\left( \frac{\partial}{\partial t} + U_o \frac{\partial}{\partial x} \right) \left( \frac{\partial^2 \psi}{\partial x^2} + \frac{\partial^2 \psi}{\partial z^2} \right) - \frac{\partial^2 U_o}{\partial z^2} \frac{\partial \psi}{\partial x} + \frac{g}{\theta_o} \frac{\partial \theta}{\partial x} = 0 . \quad (6)$$


---

We can assume the following forms for the solution of both  $\psi$  and  $\frac{\theta}{\theta_o}$ :

---


$$\begin{aligned} \psi &= \hat{\psi}(z) \operatorname{Re} [\exp \{ik(x - ct)\}] , \\ \frac{\theta}{\theta_o} &= \hat{\theta}(z) \operatorname{Re} [\exp \{ik(x - ct)\}] . \end{aligned} \quad (7)$$


---

where  $k$  is horizontal wavenumber and  $c$  is horizontal phase velocity. The imaginary part of  $c$  corresponds to the growth rate of the perturbation. Thus, we obtain the following from (4-4) and (6):

---


$$(U_o - c) \hat{\theta} - \frac{N_o^2}{g} \hat{\psi} = 0 , \quad (8-1)$$


---

$$(U_o - c) \left( \frac{\partial^2}{\partial z^2} - k^2 \right) \hat{\psi} - \frac{\partial^2 U_o}{\partial z^2} \hat{\psi} + g \hat{\theta} = 0 . \quad (8-2)$$


---

Here, we use the finite difference method for (8-1) and (8-2) to solve the matrix eigenvalue problem. The boundary condition of  $w = 0 \text{ m s}^{-1}$  is given at the upper ( $z = 20,000 \text{ m}$ ) and lower ( $z = 0 \text{ m}$ ) boundaries:

---



---


$$w = -\frac{\partial\psi}{\partial x} = 0 \rightarrow \psi = 0 \text{ at the top and bottom boundaries.} \quad (9)$$


---



---

It was confirmed that the dependence of the results on the vertical resolution is not significant. In the following, we show the results for a vertical resolution of 50 m. The most unstable mode was obtained by solving a series of matrix eigenvalue problem for fixed horizontal wavelengths ( $k$ ) of 0–8000m every 20m.

Figure 10a shows the idealized profiles of  $U_o(z)$  and  $N^2(z)$  for Case A and Case B. For Case A,  $U_o(z)$  is given by a sum of the hyperbolic-tangent shaped background wind profile having a vertical shear centered at  $z = 10.0$  km and a sinusoidal wave with maximum amplitude centered at  $z = 9.0$  km and a vertical wavelength of 2.0 km. This sinusoidal wave corresponds to the orographic GWs that likely provide strong vertical wind shear. Without this sinusoidal wave structure, the region of  $Ri < 0.25$  does not appear and unstable modes do not emerge.:

---


$$\begin{aligned}
 U_o(z) = & \quad (10) \\
 & 10 \cdot \tanh\left(\frac{(z-10.0)}{1.0}\right) - 10 \\
 & + 6.0 \cdot \\
 & \exp\left(-\frac{1}{2}\frac{(z-9)^2}{1.0}\right) \cdot \cos\left(2\pi\frac{(z-9.5)}{2.0}\right) .
 \end{aligned}$$


---



---

A constant value of  $1.0 \times 10^{-4} \text{ s}^{-2}$  is given for  $N^2(z)$ . Consequently, the most unstable mode with horizontal wavelength of  $\sim 1750$  m was obtained, which is slightly shorter and thinner than that from the PANSY radar observations. This mode has the largest amplitude at  $z \sim 8.8$  km, and its phase is shifted by  $\sim +75^\circ$  at  $z = \sim 8.8$  km.

For Case B,  $U_o$  is simply given by the hyperbolic-tangent shaped vertical shear centered at  $z = 7.5$  km. The vertical shear strength and the thickness of the unstable layer, determined from the PANSY radar observations (Figure 6a), have vertical thickness of approximately 1.0 km and shear strength of  $\sim 15 \text{ m s}^{-1} \text{ km}^{-1}$ . The same constant value of  $N^2$  is given as in Case A:

---


$$U_o(z) = -15 \cdot \tanh\left(\frac{(z-7.5)}{1.0}\right) - 15 , \quad (11)$$


---



---

For this case, the most unstable mode has horizontal wavelength of  $\sim 3600$  m, which is slightly shorter and thinner than that from the PANSY radar observations. This mode has its maximum amplitude at  $z \sim 7.5$  km, and its phase is shifted by  $\sim -60^\circ$  both above and below this level.

The horizontal wavelength and depth in Case B are longer and thicker than in Case A. The phase shift in the vertical for Case B is the opposite of that for Case

A. These characteristics are consistent with the observations, and the central altitudes of the amplitude also accord well with the observations. However, some differences are also found, i.e., the estimated most unstable modes are slightly shorter and thinner than the observations.

#### 4.2 Development Process of the Cyclone Associated with Strong Shear

We examined the temporal evolution of the cyclone that approached Syowa Station, which was strongly associated with the development of K-H billows in both Case A and Case B. The cyclone developed through baroclinic instability at around 55°S on 19–20 March; the phase lines of the pressure perturbations associated with the cyclone tilt westward with height (not shown). The amplitude maxima of the meridional wind and pressure perturbations near the surface and the tropopause (not shown) were consistent with baroclinic instability.

Figure 11a show longitude-latitude cross sections of potential temperature ( $\theta$ ) at  $z = 7.0$  km every 12 h from (1) 00:00 UTC on 20 March to (6) 12:00 UTC 22 March. A cutoff cyclone formed at  $\sim 60.0^\circ\text{S}$ ,  $\sim 35.0^\circ\text{E}$  at 00:00 UTC on 21 March. This cyclone with strong winds in the upper troposphere moved southward toward Syowa Station. It can also be seen that an air mass with high  $\theta$  from at lower latitude region was entrained into the cyclone and separated from the high  $\theta$  region at lower latitudes at 12:00 UTC on 21 March. The center of the cyclone was surrounded by the high  $\theta$  air mass above Syowa Station at 12:00 UTC on 22 March (see enlarged snapshot in Figure 11b). Figure 11c show a horizontal-height cross section of  $\theta$  and horizontal wind speed along line A–B depicted in Figure 11b. The shallow southwestward jet in the upper troposphere, observed above Syowa Station, is related to and maintained by the strong horizontal gradient of  $\theta$  through the thermal wind balance. It should be noted again that this locally enhanced southwestward jet in the upper troposphere provided the KHI conditions that caused the K-H billows in Case B.

#### 5 Summary and Concluding Remarks

We conducted two 10-day observational campaigns targeting atmospheric turbulence in the Antarctic troposphere and lower stratosphere using the PANSY radar with the FII technique and radiosondes. Such long-term and continuous observations using the FII technique of MST radars have not been performed previously. Additionally, this study was the first to undertake direct observation of K-H billows using an MST radar in the Antarctic. During the campaigns, we identified 73 cases of K-H billows visually.

On 20–23 March two strong characteristic K-H billows were detected in the upper troposphere. It was shown that the excitation mechanisms of these two cases of K-H billows over Syowa Station differed, despite both being related to the approach of a strong cyclone typical of the Antarctic coastal region. Case A was characterized by the longest duration. A long-lasting large-amplitude orographic GW was dominant during the Case A event. It is considered that this orographic GW continued to be excited over Syowa Station by strong southwestward winds near the ground associated with the cyclone, which blew up

the coastal slope of the Antarctic continent. The orographic GWs were quasi-stationary and hence continued to provide strong vertical shear in the upper troposphere that supported long duration KHI.

Case B was characterized by the deepest structure. The strong cyclone was located ~500 km northwest of Syowa Station. The shallow southward jet embedded in the cyclone provided the strong vertical shear in the upper troposphere that excited the K-H billows over Syowa Station. It was also shown that a stretched and elongated air mass with high  $\theta$ , which was formed by a strongly nonlinear process, maintained the strong jet so as to satisfy the local thermal wind balance. The vertical shear below the upper tropospheric jet had thicker structure than the phase of the orographic GWs that excited the K-H billows in Case A. The difference in the depth of the vertical shear would be the reason for the thicker structure of the K-H billows in Case B.

Using linear instability theory, we also confirmed that the observed two K-H billows were consistent with the most unstable modes in terms of the horizontal wavelength, phase shift in the vertical, and central altitude.

Orographic GWs are known to be dominant throughout the year in the troposphere over the Antarctic coastal region owing to its steep slope (e.g., Minamihara et al., 2018). It is also known that well-developed cyclones tend to approach the coastal region of the Antarctica, and frequently cause tropopause folding (Škerlak et al., 2015, Kohma et al., 2022). Thus, the two excitation mechanisms of K-H billows, illustrated by case studies described in this paper, clearly reflect the characteristics of the Antarctic coastal region and, therefore, would appear common in this region.

Statistical analysis was performed for the 73 cases of K-H billows detected in this study. Approximately 60% of cases were detected in the height region of  $z < 4.0$  km. In this height region, vertical shear was strong and  $N^2$  was small throughout the entire period. The vertical shear might correspond to the structure in the upper part of the katabatic wind blowing down the slope of the Antarctic continent. There was no distinct difference in the statistical values between cases in March and those in August. It was found that the parameters of the K-H billows obtained from the PANSY radar observations were similar to those derived from MU radar observations in the mid-latitudes (Fukao et al., 2011), except for the wave periods, which were approximately twice as long as those observed by the MU radar. The difference in the wave periods is likely explained by the difference in the strength of the background winds, which were approximately 60% weaker above Syowa Station than above the MU radar site.

In future work, additional observations will be necessary to explore the occurrence frequency of the two mechanisms elucidated by this study. It is also possible through accumulation of such observations that new excitation mechanisms for K-H billows will be discovered. The K-H billows observed in the lower troposphere were not considered fully in this study owing to their very shallow structure, but more detailed analysis is desired. It is also noteworthy that in the

field reproduced by NICAM, Ri over Syowa Station was very small at almost the same heights and times as where and when the S-shaped echo patterns were observed from PANSY radar observations. Comparison of turbulence parameters between the NICAM simulations and PANSY radar observations will be useful for improving the turbulence scheme for the free atmosphere in the model.

### Acknowledgments

This study is supported by JST CREST grant JPMJCR1663 and JSPS KAKENHI grants 201703536. PANSY is a multi-institutional project with core members from The University of Tokyo, the National Institute of Polar Research, and the Kyoto University. The PANSY radar and radiosonde measurements at Syowa Station are operated by the Japanese Antarctic Research Expedition (JARE). Operational radiosonde observation data at Syowa Station is provided by the Japan Meteorological Agency (JMA). The numerical simulations using NICAM were run on the NIPR supercomputer and the computational resource of Fujitsu PRIMERGY CX600M1/CX1640M1 (Oakforest-PACS) awarded by "Large-scale HPC Challenge" Project, Joint Center for Advanced High-Performance Computing (JCAHPC). All graphics were drawn by software developed by the Dennou Club Library (DCL). We are grateful to Hiroshi Niino at for helpful advice, Taishi Hashimoto for technical advices on FII data conversion, and Ryosuke Shibuya for valuable advices and helps on the operation of the NICAM simulations. Finally, we would like to appreciate the members of the 60th Japanese Antarctic Research Expedition (JARE 60) for their enormous support of our observations at Syowa Station.

### Open Research

The model results used to support this article can be obtained from the corresponding author upon request ([minamihara@eps.s.u-tokyo.ac.jp](mailto:minamihara@eps.s.u-tokyo.ac.jp)). The PANSY radar observational data are available at the project website: <http://pansy.eps.s.u-tokyo.ac.jp>.

**Figure 1.** Time-height cross sections of (a) echo power observed by the PANSY FII mode, (b) zonal ( $u$ ) and (c) meridional ( $v$ ) wind observed by the PANSY standard mode, and (d) vertical shear ( $|\frac{dU}{dz}|$ ), (e) squared buoyancy frequency ( $N^2$ ), and (f) Richardson number (Ri) estimated from radiosonde observations in March. In (b) and (c), the contour interval is  $10 \text{ m s}^{-1}$ .

**Figure 2.** Same as in Figure 1 but for observations in August.

**Figure 3.** Time-height cross sections of (a) echo power and (b) vertical winds ( $w$ ) observed by the PANSY FII mode for Case A. Green line shows the trajectory of the radiosonde.

**Figure 4.** Vertical profiles of (a)  $u$  and  $v$ , (b) horizontal wind disturbances ( $u'$  and  $v'$ ), (c)  $|\frac{dU}{dz}|$  observed by the PANSY standard mode at 14:01 UTC on 21 March. Vertical profiles of (d)  $N^2$  and (e) Ri observed by the radiosonde

launched at 15:30 UTC on 21 March are also shown. A hodograph of  $u'$  and  $v'$  observed by the PANSY radar for the height of  $z = 9.0\text{--}10.5$  km is shown in panel (f).

**Figure 5.** (a) Longitude-latitude cross section of horizontal wind divergence ( $\nabla_h \cdot v_h$ ) (color) and pressure ( $p$ ) (contour) at  $z = 9.5$  km with a contour interval of 2 hPa. (b) Horizontal-height cross sections of (b)  $\nabla_h \cdot v_h$  (color), (c)  $v$  (color), and (d) zonal momentum vertical fluxes ( $\overline{u'w'}$ ) (color) overlaid with horizontal wind speed (contour) along the broken line A–B shown in panel (a) with a contour interval of  $5 \text{ m s}^{-1}$ . All panels show the results of the NICAM simulation at 14:30 UTC on 21 March.

**Figure 6.** Time-height cross sections of (a) echo power and (b)  $w$  observed by the PANSY FII mode for Case B. Green line shows the trajectory of the radiosonde. (c) A detailed time-height cross section of  $w$  (color) and echo power (contour). Only contours of 55 and 60 dB are drawn.

**Figure 7.** Vertical profiles of (a)  $u$  and  $v$ , (b)  $u'$  and  $v'$ , and (c)  $|\frac{d\mathbf{U}}{dz}|$  observed by the PANSY standard mode at 12:00 UTC on 22 March. Vertical profiles of (d)  $N^2$  and (e) Ri observed by the radiosonde launched at 11:30 UTC on 22 March are also shown. Red solid line in panel (e) shows the height region in which Ri is  $< 0.25$ .

**Figure 8.** (a) Longitude-latitude cross section of  $\nabla_h \cdot v_h$  (color) and  $p$  (contour) at  $z = 7.0$  km with a contour interval of 1 hPa. (b) Horizontal-height cross sections of (b)  $v$  (color), (c)  $|\frac{d\mathbf{U}}{dz}|$  (color), and (d) Ri (color) overlaid with horizontal wind speed (contour) along the broken line A–B shown in panel (a) with a contour interval of  $5 \text{ m s}^{-1}$ . All panels show the results of the NICAM simulation at 12:30 UTC on 22 March.

**Figure 9.** (a) Histogram of the number of observed K-H billows for each height. Histograms of (b) wave period, (c) depth, (d) wavelength, and (e) aspect ratio of the K-H billows. Histograms of (f)  $|\frac{d\mathbf{U}}{dz}|$  observed by the PANSY standard mode, (g)  $N^2$ , and (h) Ri observed by the radiosondes. (i) Histogram of  $\varepsilon$  for the entire observational time-height region (gray) and  $\varepsilon$  in the region in which the K-H billows were observed (black). Mean and median values are shown in the upper-right corners of the panels.

**Figure 10.** (a) Idealized vertical profiles of  $U_o$  (black solid) and  $\frac{dU_o}{dz}$  (gray solid), (b)  $N^2$ , and (c) Ri that mimic (1) Case A and (2) Case B. (d) Growth rate versus horizontal wavelength for the unstable modes expected from linear theory. (e) Vertical profile of the normalized amplitude and phase for the most unstable mode.

**Figure 11.** Longitude-latitude cross sections of (a) potential temperature ( $\theta$ ) at  $z = 7.0$  km every 12 h from (1) 00:00 UTC on 20 March to (6) 12:00 UTC 22 March. Contours show  $p$  at  $z = 7.0$  km with an interval of 1 hPa. (b) Detailed longitude-latitude cross section of the panel (a6) and (c) horizontal-height cross section of  $\theta$  (color) and horizontal wind speed (contour) along the broken line

A–B shown in panel (b) with a contour interval of  $5 \text{ m s}^{-1}$ . Black cross indicates location of Syowa Station.

**Table 1.** List of statistical mean and median values for dynamical characteristics of the K-H billows obtained in the present study (# 73) and by the MU radar (Fukao et al., 2011).

## References

- Birner, T., Sankey, D., & Shepherd, T. G. (2006). The tropopause inversion layer in models and analyses. *Geophysical Research Letters*, *33*(14). <https://doi.org/10.1029/2006GL026549>
- Browning, K. A., & Watkins, C. D. (1970). Observations of Clear Air Turbulence by High Power Radar. *Nature* *1970* *227*:5255, *227*(5255), 260–263. <https://doi.org/10.1038/227260a0>
- Chapman, D., & Browning, K. A. (1999). Release of potential shearing instability in warm frontal zones. *Quarterly Journal of the Royal Meteorological Society*, *125*(558), 2265–2289. <https://doi.org/10.1002/QJ.49712555815>
- Chilson, P. B., Muschinski, A., & Schmidt, G. (1997). First observations of Kelvin-Helmholtz billows in an upper level jet stream using VHF frequency domain interferometry. *Radio Science*, *32*(3), 1149–1160. <https://doi.org/10.1029/97RS00088>
- Fritts, D. C. (1979). *The Excitation of Radiating Waves and Kelvin-Helmholtz Instabilities by the Gravity Wave-Critical Level Interaction*. *Journal of the Atmospheric Sciences* (Vol. 36). American Meteorological Society. [https://doi.org/10.1175/1520-0469\(1979\)036<0012:TEORWA>2.0.CO;2](https://doi.org/10.1175/1520-0469(1979)036<0012:TEORWA>2.0.CO;2)
- Fukao, S., & Hamazu, K. (2014). Radar for meteorological and atmospheric observations. *Radar for Meteorological and Atmospheric Observations*, *9784431543*, 1–537. <https://doi.org/10.1007/978-4-431-54334-3>
- Fukao, S., Luce, H., Mega, T., & Yamamoto, M. (2011). Extensive studies of large-amplitude Kelvin-Helmholtz billows in the lower atmosphere with VHF middle and upper atmosphere radar. *Quarterly Journal of the Royal Meteorological Society*, *137*(657), 1019–1041. <https://doi.org/10.1002/QJ.807>
- Geerts, B., Miao, Q., Yang, Y., Rasmussen, R., & Breed, D. (2010). An Airborne Profiling Radar Study of the Impact of Glaciogenic Cloud Seeding on Snowfall from Winter Orographic Clouds. *Journal of the Atmospheric Sciences*, *67*(10), 3286–3302. <https://doi.org/10.1175/2010JAS3496.1>
- Geerts, B., Damiani, R., & Haimov, S. (2006). Finescale Vertical Structure of a Cold Front as Revealed by an Airborne Doppler Radar. *Monthly Weather Review*, *134*(1), 251–271. <https://doi.org/10.1175/MWR3056.1>
- Gelaro, R., McCarty, W., Suárez, M. J., Todling, R., Molod, A., Takacs, L., ... Zhao, B. (2017). The Modern-Era Retrospective Analysis for Research and Applications, Version 2 (MERRA-2). *Journal of Climate*, *30*(14), 5419–5454. <https://doi.org/10.1175/JCLI-D-16-0758.1>
- Grasmick, C., & Geerts, B. (2020). Detailed Dual-Doppler Structure of Kelvin-Helmholtz Waves from an Airborne Profiling Radar over Complex Terrain. Part I: Dynamic Structure. *Journal of the Atmospheric Sciences*, *77*(5), 1761–1782. <https://doi.org/10.1175/JAS-D-19-0108.1>
- Hardy, K. R., Reed, R. J., & Mather, G. K. (1973). Observation of Kelvin-Helmholtz billows and their mesoscale environment by radar, instrumented aircraft, and a dense radiosonde

network. *Quarterly Journal of the Royal Meteorological Society*, 99(420), 279–293. <https://doi.org/10.1002/QJ.49709942007>Hocking, W. K. (1983). On the extraction of atmospheric turbulence parameters from radar backscatter Doppler spectra—I. Theory. *Journal of Atmospheric and Terrestrial Physics*, 45(2–3), 89–102. [https://doi.org/10.1016/S0021-9169\(83\)80013-0](https://doi.org/10.1016/S0021-9169(83)80013-0)Hocking, W. K. (1999). The dynamical parameters of turbulence theory as they apply to middle atmosphere studies. *Earth, Planets and Space*, 51(7–8), 525–541. <https://doi.org/10.1186/BF03353213>METRICSKantha, L., Lawrence, D., Luce, H., Hashiguchi, H., Tsuda, T., Wilson, R. J., ... Yabuki, M. (2017). Shigaraki UAV-Radar Experiment (ShUREX): overview of the campaign with some preliminary results. *Progress in Earth and Planetary Science*, 4(1), 1–26. <https://doi.org/10.1186/S40645-017-0133-X>FIGURES/23Klostermeyer, J., & Rüster, R. (1980). Radar observation and model computation of a jet stream-generated Kelvin-Helmholtz instability. *Journal of Geophysical Research: Oceans*, 85(C5), 2841–2846. <https://doi.org/10.1029/JC085IC05P02841>Kohma, M., Sato, K., Tomikawa, Y., Nishimura, K., & Sato, T. (2019). Estimate of Turbulent Energy Dissipation Rate From the VHF Radar and Radiosonde Observations in the Antarctic. *Journal of Geophysical Research: Atmospheres*, 124(6), 2976–2993. <https://doi.org/10.1029/2018JD029521>Kohma, M., Sato, K., Nishimura, K., Tsutsumi, M., & Sato, T. (2020). A Statistical Analysis of the Energy Dissipation Rate Estimated From the PMWE Spectral Width in the Antarctic. *Journal of Geophysical Research: Atmospheres*, 125(16), e2020JD032745. <https://doi.org/10.1029/2020JD032745>Luce, H., Yamamoto, M., Fukao, S., Helal, D., & Crochet, M. (2001). A frequency domain radar interferometric imaging (FII) technique based on high-resolution methods. *Journal of Atmospheric and Solar-Terrestrial Physics*, 63(2–3), 221–234. [https://doi.org/10.1016/S1364-6826\(00\)00147-4](https://doi.org/10.1016/S1364-6826(00)00147-4)Luce, H., Kantha, L., Hashiguchi, H., Lawrence, D., & Doddi, A. (2018). Turbulence kinetic energy dissipation rates estimated from concurrent UAV and MU radar measurements. *Earth, Planets and Space*, 70(1), 1–19. <https://doi.org/10.1186/S40623-018-0979-1>FIGURES/15Luce, H., Hassenpflug, G., Yamamoto, M., & Fukao, S. (2006). High-resolution vertical imaging of the troposphere and lower stratosphere using the new MU radar system. *Annales Geophysicae*, 24(3), 791–805. <https://doi.org/10.5194/ANGE0-24-791-2006>Luce, H., Hassenpflug, G., Yamamoto, M., Crochet, M., & Fukao, S. (2007). Range-imaging observations of cumulus convection and Kelvin-Helmholtz instabilities with the MU radar. *Radio Science*, 42(1), n/a-n/a. <https://doi.org/10.1029/2005RS003439>Luce, H., Hassenpflug, G., Yamamoto, M., Fukao, S., & Sato, K. (2008). High-Resolution Observations with MU Radar of a KH Instability Triggered by an Inertia-Gravity Wave in the Upper Part of a Jet Stream. *Journal of the Atmospheric Sciences*, 65(5), 1711–1718. <https://doi.org/10.1175/2007JAS2346.1>Mahalov, A., Moustouli, M., Nicolaenko, B., & Tse, K. L. (2007). Computational studies of inertia-gravity waves radiated from upper tropospheric jets. *Theoretical and Computational Fluid Dynamics 2007 21:6*, 21(6), 399–422. <https://doi.org/10.1007/S00162-007-0062-1>Medina, S., & Houze, R. A. (2016). Kelvin-Helmholtz waves in extratropical cyclones passing over mountain ranges.

*Quarterly Journal of the Royal Meteorological Society*, 142(696), 1311–1319. <https://doi.org/10.1002/QJ.2734>Miles, J. W., & Howard, L. N. (1964). Note on a heterogeneous shear flow. *Journal of Fluid Mechanics*, 20(2), 331–336. <https://doi.org/10.1017/S0022112064001252>Minamihara, Y., Sato, K., Tsutsumi, M., & Sato, T. (2018). Statistical Characteristics of Gravity Waves With Near-Inertial Frequencies in the Antarctic Troposphere and Lower Stratosphere Observed by the PANSY Radar. *Journal of Geophysical Research: Atmospheres*, 123(17), 8993–9010. <https://doi.org/10.1029/2017JD028128>Minamihara, Y., Sato, K., & Tsutsumi, M. (2020). Intermittency of Gravity Waves in the Antarctic Troposphere and Lower Stratosphere Revealed by the PANSY Radar Observation. *Journal of Geophysical Research: Atmospheres*, 125(15), e2020JD032543. <https://doi.org/10.1029/2020JD032543>Nastrom, G. D., & Eaton, F. D. (1997). Turbulence eddy dissipation rates from radar observations at 5–20 km at White Sands Missile Range, New Mexico. *Journal of Geophysical Research: Atmospheres*, 102(D16), 19495–19505. <https://doi.org/10.1029/97JD01262>Nishimura, K., Kohma, M., Sato, K., & Sato, T. (2020). Spectral Observation Theory and Beam Debroadening Algorithm for Atmospheric Radar. *IEEE Transactions on Geoscience and Remote Sensing*, 58(10), 6767–6775. <https://doi.org/10.1109/TGRS.2020.2970200>Palmer, R. D., Yu, T. Y., & Chilson, P. B. (1999). Range imaging using frequency diversity. *Radio Science*, 34(6), 1485–1496. <https://doi.org/10.1029/1999RS900089>Petre, J. M., & Verlinde, J. (2004). Cloud Radar Observations of Kelvin–Helmholtz Instability in a Florida Anvil. *Monthly Weather Review*, 132(10), 2520–2523.Plougonven, R., Hertzog, A., & Guez, L. (2013). Gravity waves over Antarctica and the Southern Ocean: consistent momentum fluxes in mesoscale simulations and stratospheric balloon observations. *Quarterly Journal of the Royal Meteorological Society*, 139(670), 101–118. <https://doi.org/10.1002/QJ.1965>Ralph, F. M., Neiman, P. J., Keller, T. L., Levinson, D., & Fedor, L. (1997). Observations, Simulations, and Analysis of Nonstationary Trapped Lee Waves. *Journal of the Atmospheric Sciences*, 54(10), 1308–1333. [https://doi.org/10.1175/JAS-D-16-0145.1](https://doi.org/10.1175/1520-0469(1997)054Samelson, R. M., & Skillingstad, E. D. (2016). Frontogenesis and Turbulence: A Numerical Simulation. <i>Journal of the Atmospheric Sciences</i>, 73(12), 5025–5040. <a href=)Sassen, K. (2002). Indirect climate forcing over the western US from Asian dust storms. *Geophysical Research Letters*, 29(10), 1031–1034. <https://doi.org/10.1029/2001GL014051>Sato, K. (1994). A statistical study of the structure, saturation and sources of inertio-gravity waves in the lower stratosphere observed with the MU radar. *Journal of Atmospheric and Terrestrial Physics*, 56(6), 755–774. [https://doi.org/10.1016/0021-9169\(94\)90131-7](https://doi.org/10.1016/0021-9169(94)90131-7)Sato, K., Tsutsumi, M., Sato, T., Nakamura, T., Saito, A., Tomikawa, Y., ... Yamanouchi, T. (2014). Program of the Antarctic Syowa MST/IS radar (PANSY). *Journal of Atmospheric and Solar-Terrestrial Physics*, 118, 2–15. <https://doi.org/10.1016/J.JASTP.2013.08.022>Sato, T., & Woodman, R. F. (1982). Fine Altitude Resolution Observations of Stratospheric Turbulent Layers by the Arecibo 430 MHz Radar. *Journal*

of *Atmospheric Sciences*, 39(11), 2546–2552. [https://doi.org/10.1175/1520-0469\(1982\)039<2546:FAROOS>2.0.CO;2](https://doi.org/10.1175/1520-0469(1982)039<2546:FAROOS>2.0.CO;2)Satoh, M., Matsuno, T., Tomita, H., Miura, H., Nasuno, T., & Iga, S. (2008). Nonhydrostatic icosahedral atmospheric model (NICAM) for global cloud resolving simulations. *Journal of Computational Physics*, 227(7), 3486–3514. <https://doi.org/10.1016/J.JCP.2007.02.006>Satoh, M., Tomita, H., Yashiro, H., Miura, H., Kodama, C., Seiki, T., ... Kubokawa, H. (2014). The Non-hydrostatic Icosahedral Atmospheric Model: description and development. *Progress in Earth and Planetary Science 2014 1:1*, 1(1), 1–32. <https://doi.org/10.1186/S40645-014-0018-1>Schneider, A., Gerding, M., & Lübken, F. J. (2015). Comparing turbulent parameters obtained from LITOS and radiosonde measurements. *Atmospheric Chemistry and Physics*, 15(4), 2159–2166. <https://doi.org/10.5194/ACP-15-2159-2015>Scorer, R. S. (1969). *Billow mechanics* (Vol. 4). <https://doi.org/10.1029/RS004i012p01299>Shibuya, R., & Sato, K. (2019). A study of the dynamical characteristics of inertia-gravity waves in the Antarctic mesosphere combining the PANSY radar and a non-hydrostatic general circulation model. *Atmospheric Chemistry and Physics*, 19(5), 3395–3415. <https://doi.org/10.5194/ACP-19-3395-2019>Shibuya, R., Miura, H., & Sato, K. (2016). A Grid Transformation Method for a Quasi-Uniform, Circular Fine Region Using the Spring Dynamics. *Journal of the Meteorological Society of Japan. Ser. II*, 94(5), 2016–022. <https://doi.org/10.2151/JMSJ.2016-022>Škerlak, B., Sprenger, M., Pfahl, S., Tyrllis, E., & Wernli, H. (2015). Tropopause folds in ERA-Interim: Global climatology and relation to extreme weather events. *Journal of Geophysical Research: Atmospheres*, 120(10), 4860–4877. <https://doi.org/10.1002/2014JD022787>Takayabu, I. (1992). Kelvin-Helmholtz Billow Clouds on a Frontal Surface. *Journal of the Meteorological Society of Japan. Ser. II*, 70(2), 733–738. [https://doi.org/10.2151/JMSJ1965.70.2\\_733](https://doi.org/10.2151/JMSJ1965.70.2_733)Theuerkauf, A., Gerding, M., & Lübken, F. J. (2011). LITOS - A new balloon-borne instrument for fine-scale turbulence soundings in the stratosphere. *Atmospheric Measurement Techniques*, 4(1), 55–66. <https://doi.org/10.5194/AMT-4-55-2011>Tomikawa, Y., Nishimura, Y., & Yamanouchi, T. (2009). Characteristics of Tropopause and Tropopause Inversion Layer in the Polar Region. *SOLA*, 5(1), 141–144. <https://doi.org/10.2151/SOLA.2009-036>Tomita, H., & Satoh, M. (2004). A new dynamical framework of nonhydrostatic global model using the icosahedral grid. *Fluid Dynamics Research*, 34(6), 357–400. <https://doi.org/10.1016/J.FLUIDDYN.2004.03.003>XMLTrier, S. B., Sharman, R. D., MuñOz-Esparza, D., & Lane, T. P. (2020). Environment and Mechanisms of Severe Turbulence in a Midlatitude Cyclone. *Journal of the Atmospheric Sciences*, 77(11), 3869–3889. <https://doi.org/10.1175/JAS-D-20-0095.1>VanZandt, T. E., Green, J. L., Clark, W. L., & Grant, J. R. (1979). Buoyancy waves in the troposphere: Doppler radar observations and a theoretical model. *Geophysical Research Letters*, 6(6), 429–432. <https://doi.org/10.1029/GL006I006P00429>Wakimoto, R. M., Blier, W., & Liu, C. (1992). The Frontal Structure of an Explosive Oceanic Cyclone: Airborne Radar Observations of ERICA IOP 4. *Monthly Weather Review*, 120(7),

1135–1155. NCEP, 2000: NCEP FNL operational model global tropospheric analyses, continuing from July 1999. National Center for Atmospheric Research Computational and Information Systems Laboratory, accessed 3 April 2017, <https://doi.org/10.5065/D6M043C6>.